


# Synthesis, Characterization and Thermal Stability of Nanocrystalline MgAlMnFeCu Low-Density High-Entropy Alloy

Vivek Kumar Pandey<sup>1</sup>  · Yagnesh Shadangi<sup>1</sup> · Vikas Shivam<sup>1</sup> · Joysurya Basu<sup>1</sup> · Kausik Chattopadhyay<sup>1</sup> · Bhaskar Majumdar<sup>2</sup> · B. N. Sarma<sup>1</sup> · Nilay Krishna Mukhopadhyay<sup>1</sup>

Received: 18 September 2020 / Accepted: 20 October 2020 / Published online: 9 November 2020  
© The Indian Institute of Metals - IIM 2020

**Abstract** An equiatomic quinary MgAlMnFeCu high-entropy alloy (HEA) has been synthesized successfully by mechanical alloying (MA). Phase evolution of MgAlMnFeCu HEA has been studied using X-ray diffraction (XRD), transmission electron microscopy (TEM) and energy-dispersive spectroscopy (EDS/XEDS). Milling up to 60 h leads to the formation of a mixture of two phases consisting of a BCC phase ( $a = 2.87 \pm 0.02 \text{ \AA}$ ) and  $\gamma$ -brass-type phase ( $a = 8.92 \pm 0.03 \text{ \AA}$ ), with  $\sim 2 \mu\text{m}$  powder particle size. The as-milled alloy after spark plasma sintering (SPS) at 900 °C exhibits an experimental density of  $4.946 \pm 0.13 \text{ g cc}^{-1}$ , which is 99.80% of the theoretical density. SPS leads to the formation of C15 Laves phase (MgCu<sub>2</sub>-type;  $a = 7.034 \pm 0.02 \text{ \AA}$ ) and B2 (AlFe-type;  $a = 2.89 \pm 0.02 \text{ \AA}$ ) intermetallic along with the  $\gamma$ -brass-type phase. The SPSed sample has exceptional hardness value ( $\sim 5.06 \text{ GPa}$ ), high compressive strength ( $\sim 1612 \text{ MPa}$ ) and appreciable failure strain ( $\sim 6.4\%$ ) coupled with relatively low density. Various thermodynamic parameters have been considered for understanding the phase evolution and their stability during MA.

**Keywords** High-entropy alloy · Phase evolution · Spark plasma sintering · Low-density HEA · Mechanical properties

## 1 Introduction

The ever-increasing demand for structural materials with high strength-to-weight ratio has dawned new horizons in alloy design and development strategies and the search has been extended into multicomponent alloys too. The search for multicomponent alloys with elements in equiatomic or near-equiatomic proportions has led to the conceptualization of high-entropy alloys (HEAs) with high strength-to-weight ratio in conjunction with other associated properties [1, 2]. Somewhat a dramatic resurgence in the design and development of HEAs with Al, Fe and Mg, etc., has been observed in the recent past [3–7]. The alloys having more than five principal alloying elements in equiatomic or near-equiatomic proportions (5 to 35 at %) often lead to the formation of a single disordered solid solution [7]. The high entropy of mixing in these alloys is primarily said to be responsible for lowering the free energy and often that dominates over the enthalpy of mixing that stabilizes a solid solution phase with BCC, FCC or HCP crystal structure [7]. It is pertinent to point out that single-phase high-entropy intermetallics of MgZn<sub>2</sub>-type Laves phase has been recently reported in TiVCrNiZr equiatomic alloy [8]. Although it is postulated that a single-phase solid solution may be formed due to the high entropy of mixing, it may not always be possible to obtain the single phase in the multicomponent alloys in cases when the enthalpy effects dominate. The first equiatomic HEA was reported by Cantor et al. [1] in the CrMnFeCoNi system with a single-phase FCC structure, although all the elements used were not having FCC structure. A careful inspection of the literature suggests that the CrFeCoNiCu and AlCrFeCoNi HEAs with FCC and BCC structure, respectively, have been studied extensively [9–16].

✉ Vivek Kumar Pandey  
vivek.rs.met13@itbhu.ac.in; miet.vivek@gmail.com

<sup>1</sup> Department of Metallurgical Engineering, Indian Institute of Technology (BHU), Varanasi, Uttar Pradesh 221005, India

<sup>2</sup> Defence Institute of Advanced Technology (DIAT), Pune 411025, India

Significant progress has been made in studying HEAs based on the transition series elements with and without the addition of Al [17, 18]. Although Mg is the lightest and cost-effective element available for structural applications, there is only limited literature on its effect on the HEAs [19–27]. Considerable efforts were made by Li et al. [24, 25] to study the impact of Mg addition in the  $Mg_x(-MnAlZnCu)_{100-x}$  ( $x = 20, 33, 43, 45.6, 50$  at %) HEAs on their microstructures, bulk densities and mechanical properties. The as-cast HEA prepared by induction melting had an HCP structure with Al–Mn-based icosahedral precipitates embedded in the matrix. These Mg-based HEAs exhibited low density in the range from 4.29 to 2.20 g cc<sup>-1</sup>, high hardness (4.29–1.78 GPa) and high compressive strength (from 500 to 400 MPa) at room temperature. However, the failure strain of these HEAs was in the range of ~ 3–5%. These HEAs had excellent thermal stability. In particular, the  $Mg_{20}(MnAlZnCu)_{80}$  HEA had shown very good thermal stability up to 677 °C (950 K). Chen et al. [27] reported the formation of amorphous phases during mechanical alloying (MA) of BeMg–TiCo and BeMgTiCoZn HEAs with all HCP elements. In another investigation, Youssef et al. [21] reported the formation of lightweight single-phase FCC structure in  $Al_{20}Li_{20}Mg_{10}Sc_{20}Ti_{30}$  HEA subjected to MA for 16 h. The MA led to the formation of nanocrystalline HEA with grain size and hardness of ~ 12 nm and ~ 5.8 GPa, respectively. After annealing at 500 °C (773 K) for 1 h, these alloys had appreciable grain growth to 26 nm and hardness up to 4.9 GPa. During annealing, these HEAs transformed from FCC to HCP structure with *c/a* ratio of 1.588.

Sanchez et al. [28] reported the formation of low-density HEA (LDHEA) by die casting in  $Al_{60}Cu_{10}Fe_{10}Cr_5Mn_5Ni_5Mg_5$  alloy having low density (4.6 g cc<sup>-1</sup>) and high hardness of 9.16 GPa. The high values of microhardness in these LDHEAs were due to the formation of complex intermetallics during die casting. Senkov et al. [29, 30] reported TiVCrZrNb low-density refractory high-entropy alloy (6.57 g cc<sup>-1</sup>) having high yield strength at room temperature (1298 MPa) and at 1000 °C (259 MPa). Stepanov et al. [31, 32] prepared lightweight AlTiVNb (5.59 g cc<sup>-1</sup>) quaternary high-entropy alloy having a single BCC phase. The prepared alloy had a compressive yield strength of 1020 MPa at room temperature and 685 MPa at 800 °C. Kumar and co-workers [33–35] made significant efforts in studying the effect of Mg addition in the HEA formation. Maulik and Kumar [34] reported the formation of HEAs with two phases during the mechanical alloying of AlFeCuCrMg<sub>*x*</sub> ( $x = 0, 0.5, 1.0, 1.7$  at %). The alloys AlCrFeCu and AlFeCuCrMg<sub>0.5</sub> subjected to MA for 20 h formed a major BCC phase with a minor FCC phase. Similarly, AlMgCrFeCu and AlFeCuCrMg<sub>1.7</sub> alloys was observed to contain two BCC phases. The dynamic DSC

thermogram confirmed the thermal stability of these alloys up to 500 °C (773 K). Maulik et al. [35] reported the detailed structural evolution of phases during spark plasma sintering (SPS) of these Mg-based HEAs. They observed the formation of AlFe, MgCu<sub>2</sub> and Mg<sub>2</sub>Cu along with the disordered BCC phase. However, the phase fraction of the intermetallic phases was dependent on the composition of the HEAs. The AlFe was the primary phase for AlFeCuCrMg<sub>1.7</sub> HEA SPSed at 800 °C along with the other minor phases, i.e. MgCu<sub>2</sub> and Mg<sub>2</sub>Cu. Kanchandani et al. [33] carried out MA of AlMgFeCuCrNi<sub>4.75</sub> alloy for 20 h for the synthesis of nanocrystalline HEA with BCC (major) and FCC (minor) phases. They also reported the effect of sintering at 900 °C on the phase evolution of these HEAs. After sintering, the BCC and FCC phases transformed into Ni<sub>3</sub>Al-type ordered phase having an excellent hardness of 4.24 GPa, which was higher than that of INCONEL 718. Li et al. [23] attempted to develop CaMgZnSrYb HEA–bulk metallic glass for a biomedical application having superior mechanical properties and better corrosion resistance compared to their conventional counterparts.

In the present work, MA has been used for the synthesis of MgAlMnFeCu HEA. The MA is the most preferred technique in this case, as the positive enthalpy of mixing between individual elements, as can be seen from calculations based on the Miedema model [36], may result in segregation or clustering in as-cast samples. The effect of Mg addition on phase evolution in this HEA has been studied carefully through XRD and TEM. A detailed investigation has been carried out to study the phase evolution after SPS of MgAlMnFeCu HEA. The effect of Mg addition on solid solution formation has been discussed based on thermodynamical calculations.

## 2 Experimental Details

The synthesis of MgAlMnFeCu HEA was accomplished by using elemental powders (325 mesh sizes) of Al, Cu, Fe, Mg and Mn having high purity, above 99.5 wt %. The physical properties and structural parameters of the individual elements are given in Table 1. A mixture of these powders taken in equiatomic proportion was milled at room temperature in a high energy planetary-type ball mill (Retsch, PM 400/2) with a ball-to-powder weight ratio of 10:1 at 200 rpm. The vials and balls were made of tungsten carbide with toluene as a process control reagent. The powders were milled up to a total of 60 h duration. The milled samples were collected after milling duration of 5, 10, 20, 30, 40, 50 and 60 h. The milled powders were characterized to find out the sequence of structural evolution and the extent of alloying in MgAlMnFeCu HEA

**Table 1** Physical property of elements in MgAlMnFeCu high-entropy alloy

|  | Al                | Cu                | Fe                | Mn                | Mg                       |
|--|-------------------|-------------------|-------------------|-------------------|--------------------------|
| Atomic radius (Å)  | 1.43              | 1.28              | 1.27              | 1.40              | 1.60                     |
| Melting point (°C)   | 660               | 1084              | 1536              | 1244              | 650                      |
| Crystal structure  | FCC               | FCC               | BCC               | Complex cubic     | HCP                      |
| Standard lattice parameter (Å)                               | 4.05              | 3.61              | 2.86              | 8.89              | $a = 3.2$ ;<br>$c = 5.2$ |
| Density (g.cm <sup>-3</sup> )                                | 2.70              | 8.96              | 7.87              | 7.40              | 1.74                     |
| Self-diffusion coefficient (m <sup>2</sup> s <sup>-1</sup> ) | 10 <sup>-19</sup> | 10 <sup>-27</sup> | 10 <sup>-31</sup> | 10 <sup>-36</sup> | 10 <sup>-13</sup>        |

powder. The phase evolution during various stages of MA was traced by X-ray diffraction (XRD) analysis, which was performed using an analytical (Empyrean) diffractometer with Co-K $\alpha$  radiation ( $\lambda = 0.179$  nm) operated at 40 kV/40 mA and at a scanning speed of 10 degree min<sup>-1</sup>. The average crystallite size and lattice strain of the MgAlMn-FeCu HEA powder were determined from the full width at half maximum (FWHM) of diffraction peaks, using Williamson and Hall method [37] after removing the instrumental broadening. The thermal stability of MA powder of MgAlMnFeCu HEA was studied using differential scanning calorimetry (DSC 404 F3, Pegasus, Netzsch) under the nitrogen atmosphere, with a heating rate of 50 K min<sup>-1</sup>. The sample was heat treated at 400 °C and 600 °C, respectively. The morphology of milled HEA powder was examined using a scanning electron microscope (NOVA NanoSEM 450, FEI) operated at 30 kV and equipped with an energy-dispersive X-ray spectrometer. The microstructural features of the MA MgAlMnFeCu HEA powder were examined using a transmission electron microscope (TECNAI G<sup>2</sup> 20, FEI) operating at 200 kV.

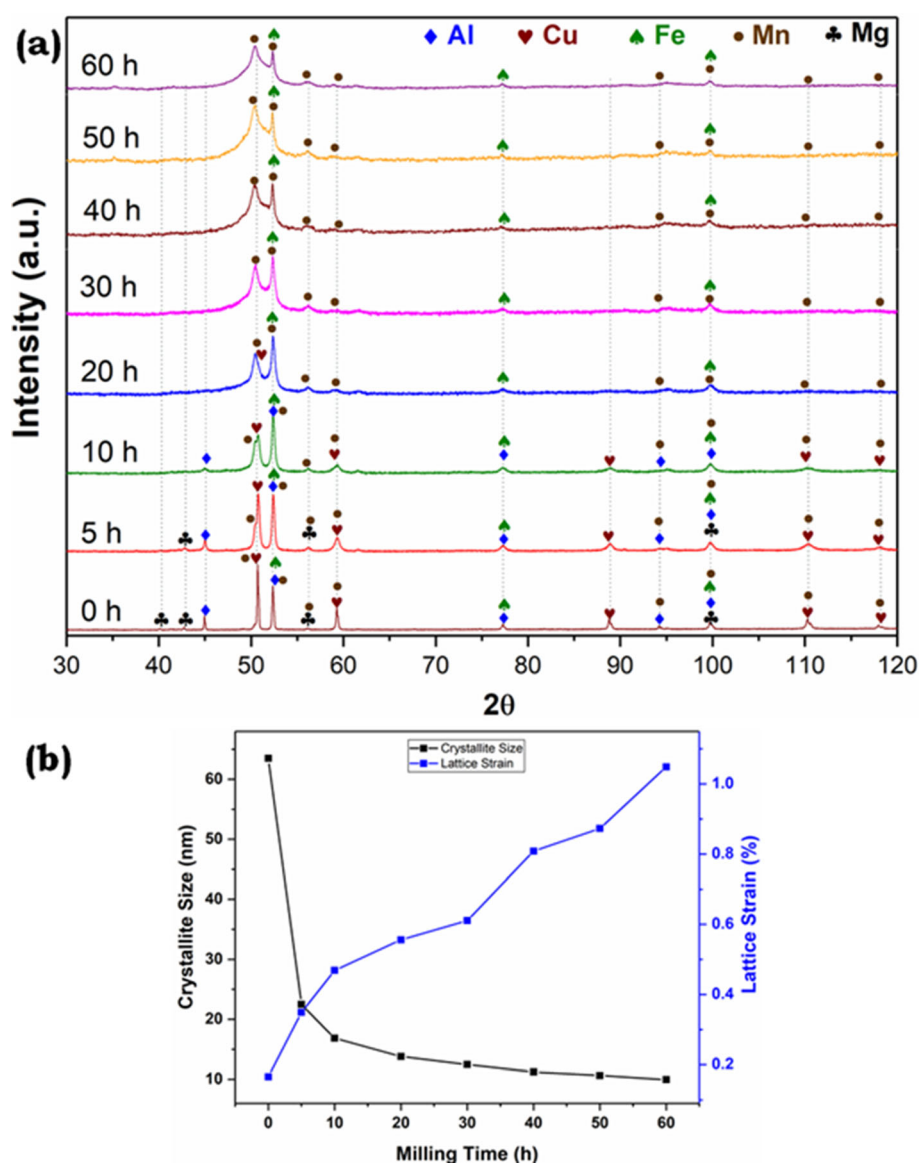
The MA MgAlMnFeCu HEA powder was consolidated using SPS at 900 °C (1173 K) using a pressure of 50 MPa with a holding time of 15 min. The density of the sintered samples was measured using Archimedes' principle. The morphology and elemental distribution of the elements within the sintered sample were examined through SEM (FEI Quanta 200F 20 kV). The bulk hardness of the SPSed sample of MgAlMnFeCu HEA was measured using a Vickers hardness tester (LECO LV700AT) at the load of 98 N with a dwell time of 10 s. Five to ten readings were taken corresponding to each measurement in order to compute the standard deviation. Microhardness tester (LM-248AT; LECO) was used to determine the microhardness of the SPSed sample at an applied load of 430 mN with a dwell time of 5 s. The compressive strength of MgAlMn-FeCu HEA after SPS was determined using a 100 kN Universal Testing Machine (Model 4206, Instron). The compression testing was performed at room temperature on

cylindrical specimens prepared as per the ASTM E9-89a specification at a strain rate of  $1.8 \times 10^{-3}$  s<sup>-1</sup>.

### 3 Results

Figure 1 shows the phase evolution during the MA of MgAlMnFeCu HEA for different milling periods up to 60 h. The diffraction peaks corresponding to all alloying elements in the pre-mixed powders can be predominantly observed. The peak intensities corresponding to various elements are different due to variations in the atomic scattering factor of each component in the HEA. Milling for 5 h leads to the broadening of peaks and reduction in the diffraction intensities corresponding to all the elements. Further, the peak corresponding to (002) reflection of Mg disappears. Milling for 10 h leads to the disappearance of all the reflections corresponding to Mg, while the intensity of peaks corresponding to (111), (220) and (311) reflections of Al, and (111) reflections of Cu decreases significantly. It has been observed that the diffraction peaks corresponding to Mg disappear earlier than those corresponding to the other elements. The intensity of the peak corresponding to (111) reflection of Cu further decreases while the high angle diffraction peaks of Cu corresponding to the (220), (311) and (222) reflections disappear after 20 h of milling. Further, milling the MgAlMnFeCu HEA up to 30 h leads to the complete dissolution of Cu in the solid solution. After 30 h of milling, all the diffraction peaks could be indexed to a BCC phase, which is quite proximate with the  $\alpha$ -Fe; and a  $\gamma$ -brass-type of phase (which is quite similar to the  $\alpha$ -Mn). Milling up to 60 h of duration was carried out in order to study further transformations in BCC and  $\gamma$ -brass-type phases, which may lead to the formation of a single-phase solid solution. A minor phase corresponding to Mn during the MA of AlCoCrFeMnNi HEA up to 30 h of milling was also reported by Shivam et al. [9]. Increasing the duration of milling up to 60 h leads to further grain refinement with no

**Fig. 1** **a** Phase evolution during mechanical alloying of MgAlMnFeCu high-entropy alloy up to 60 h of MA; **b** variation in crystallite size and lattice strain as a function of milling duration for BCC phase



appreciable change in the positions of the peaks. The milling was continued up to 60 h, and it is evident from Fig. 1 that the principal diffraction peaks of Mn, namely (411) ( $d \sim 2.10 \text{ \AA}$ ), (332) ( $d \sim 1.90 \text{ \AA}$ ), (422) ( $d \sim 1.82 \text{ \AA}$ ), (510) ( $d \sim 1.75 \text{ \AA}$ ), have broadened significantly while the diffraction peaks corresponding to minor reflections, namely (721), (730), (741) and (831), have almost disappeared. However, after 60 h of milling, a considerable broadening of diffraction peaks is observed due to the enhanced grain refinement. The signature of broadening is most significant, corresponding to the following reflections of Fe: (110) ( $d \sim 2.03 \text{ \AA}$ ), (200) ( $d \sim 1.43 \text{ \AA}$ ) and (211) ( $d \sim 1.17 \text{ \AA}$ ).

Figure 1 indicates the presence of two phases in the MgAlMnFeCu HEA, one phase consisting of a BCC solid solution formed by the dissolution of most of the elements

along with another phase corresponding to the complex cubic structure of close to  $\gamma$ -brass-type structure. The lattice parameter of the BCC phase as measured from the XRD pattern is  $a = 2.87 \pm 0.02 \text{ \AA}$ , comparable to that of  $\alpha$ -Fe, which may appear to act as host lattice. On the other hand, the lattice parameter of  $\gamma$ -brass-type phase is  $a = 8.92 \pm 0.03 \text{ \AA}$ , which is comparable to that of  $\alpha$ -Mn (cf. Table 1). It is evident from the XRD data of Fig. 1 that the intensity of the diffraction peaks corresponding to the individual elements decreases accompanied by broadening of the peaks with increasing milling duration. The latter effect is due to a decrease in the crystallite size and an increase in the lattice strain, as given in Table 2. This increase in lattice strain can be attributed to the fact that elements having atomic radii in the range from 1.27 to 1.60  $\text{\AA}$  are getting accommodated in the host lattice coupled

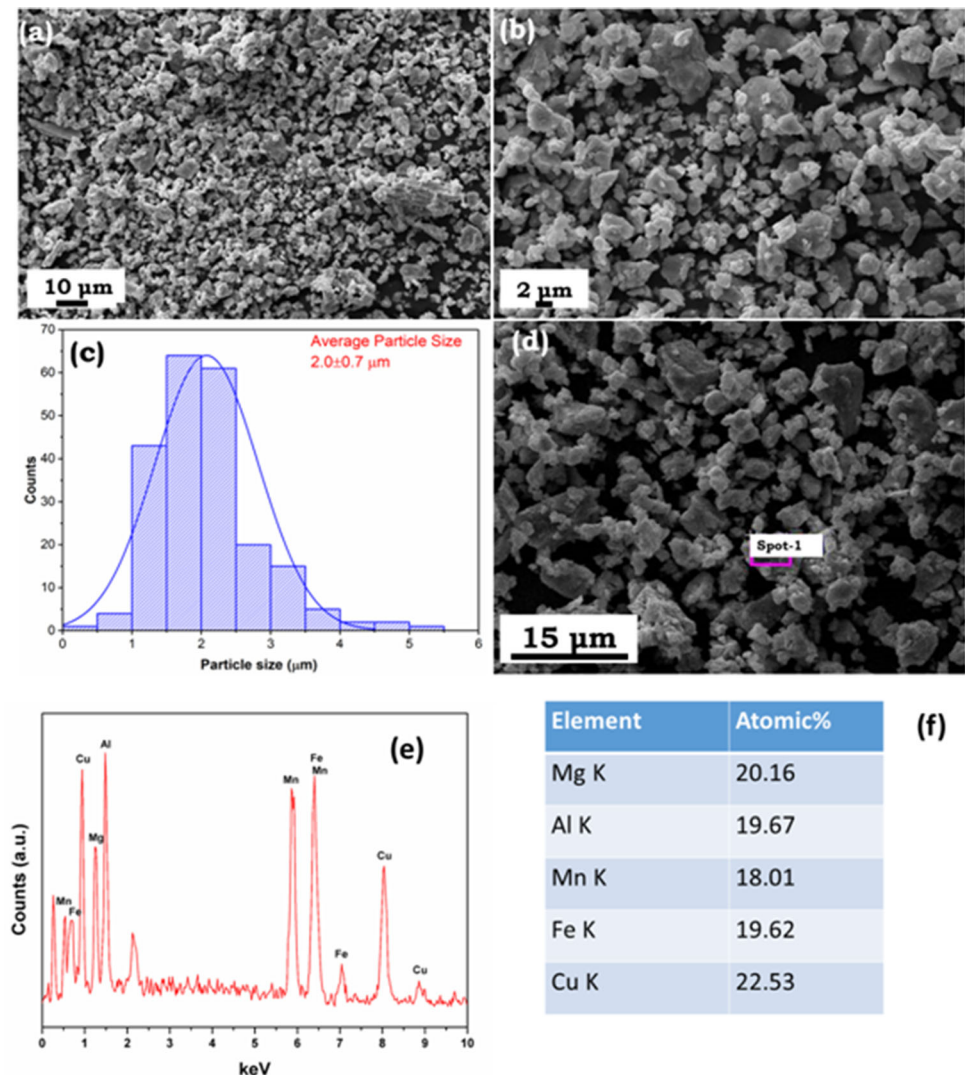
**Table 2** The crystallite size and lattice strain for BCC phase of equiatomic MgAlMnFeCu high-entropy alloy powder

| Milling time (h)      | 5    | 10   | 20   | 30   | 40   | 50   | 60   |
|-----------------------|------|------|------|------|------|------|------|
| Crystallite size (nm) | 23   | 17   | 14   | 12   | 11   | 11   | 10   |
| Lattice strain (%)    | 0.34 | 0.46 | 0.55 | 0.61 | 0.81 | 0.87 | 1.04 |

with severe plastic deformation of the powders occurring during the MA process. The formation of two solid solutions, i.e. BCC and  $\gamma$ -brass-type phase, which can be considered as solid solution of  $\alpha$ -Mn, is found to be complete after 40 h of milling. MA is, however, continued up to 60 h in order to investigate whether the  $\gamma$ -brass-type phase would dissolve into the BCC phase due to continued milling. However, no further phase transformation is observed, nor the  $\gamma$ -brass-type phase got entirely dissolved in the BCC phase.

The morphology of 60 h MA HEA is shown in Fig. 2a–b. It is observed that the shapes of the MA powder particles are irregular and in the size range of 1 to 4  $\mu\text{m}$ . In Fig. 2a–b, river-like flow patterns are often observed on the surface of the particles, which are a signature of cleavage fracture that may have arisen due to the repetitive cold welding and fracturing of the elemental powders used for making the HEA. The particle size distribution of 60 h milled powder is given in Fig. 2c, from which it is evident that the average particle size of the 60 h milled powder is  $\sim 2.0 \pm 0.7$

**Fig. 2** SEM micrograph of MgAlMnFeCu HEA MA for 60 h **a** at low magnification showing river-like pattern and; **b** at high magnification; **c** particle size distribution of MgAlMnFeCu HEA MA for 60 h; **d** spot-1 depicting the area used for collecting the chemical composition of HEA MA for 60 h; **e** EDS spectrum corresponding to spot-1 and **f** chemical composition of HEA MA for 60 h

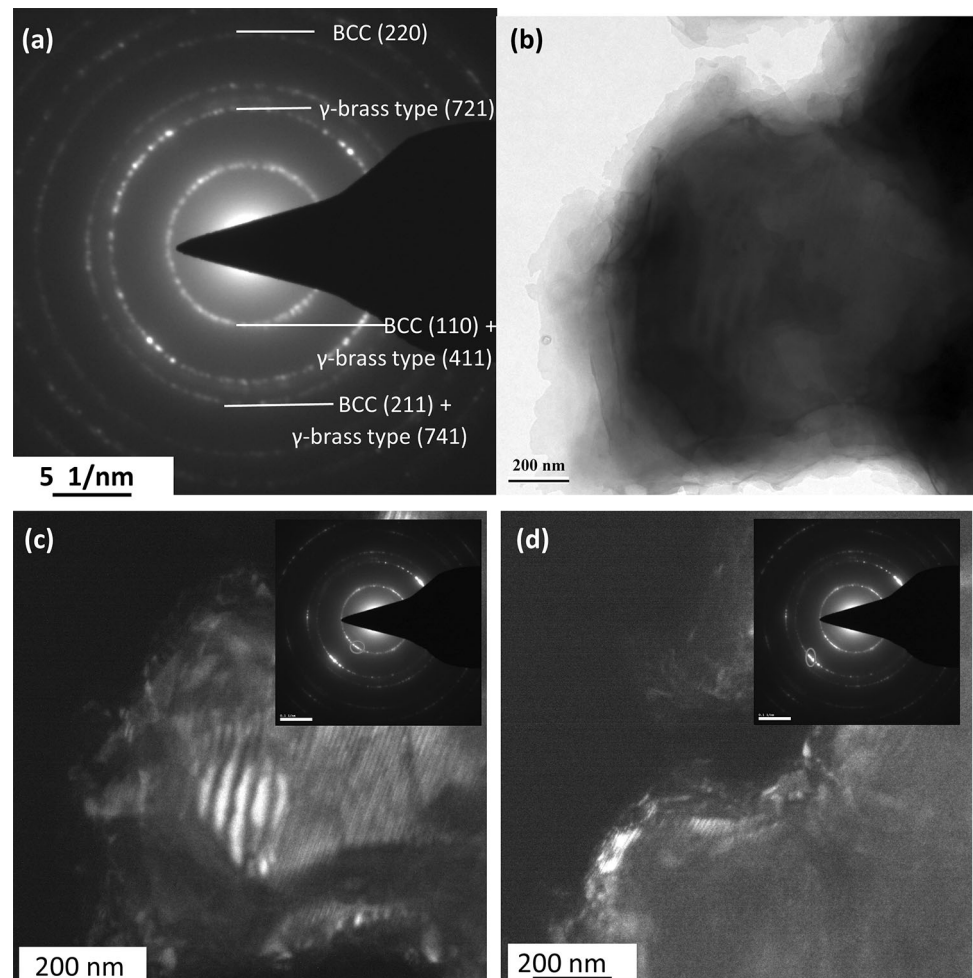


$\mu\text{m}$ . The elemental mapping of the 60 h milled MgAlMn-FeCu HEA powder sample obtained from SEM–EDS is given in Fig. 2d–e. Figure 2d shows the targeted powder particle that has been analytically mapped for obtaining the chemical composition of the HEA sample. The chemical composition and EDS spectrum of the HEA powder particle, as obtained from spot-1 in Fig. 2d, are shown in Fig. 2e. It is evident from the spectrum that the elements are uniformly distributed on a micrometre length scale. The minor variation in chemical composition from the nominal composition may be arising due to variations in the interaction volume of the electron beam with particles owing to variation in the thickness.

The microstructures of the BCC and  $\gamma$ -brass-type phases were investigated in a detailed fashion using TEM, as shown in Fig. 3. The selected area diffraction (SAD) pattern, corresponding bright field (BF) and dark field (DF) images predominantly from the BCC phase are shown in Fig. 3a–d, respectively. The SAD patterns indicate the presence of randomly oriented nanocrystalline alloy particles of the two phases mentioned earlier. Figure 3a represents all the reflections corresponding to the BCC and  $\gamma$ -

brass-type phases, which are also seen in the XRD patterns in Fig. 1. It can be confirmed that no other intermetallics are detected other than these two phases in the milled samples. The DF image corresponding to (110) reflection of the BCC phase shows the presence of elongated particles forming due to repeated cold welding and fracturing of HEA powder particles. The widely spaced parallel fringes that are seen in the dark field image in Fig. 3c could be indicative of the presence of planar faults and the appearance of Moire fringes due to the positioning of two crystallite with very similar crystallography. These parallel fringes should not be confused with phase separation. In phase separation, the phases must be interconnected, which is not observed in the present system. The interface between the two phases should be strain-free as both the phases are coherent. From the diffused ring (SADP), it can be understood that phases are not strain-free. Both BCC and  $\gamma$ -brass-type phases have fewer slip systems. Thus, the formation of planer defects is a more common phenomenon after 60 h mechanical milling. The appearance of fringes is more likely from the array of planer defects rather than phase separating domain.

**Fig. 3** **a** Selected area diffraction pattern (SADP) of BCC +  $\gamma$ -brass HEA powder particle; **b** bright field image corresponding to SADP in Fig. 3a; **c** dark field image of corresponding to BCC (110); **d** dark field image corresponding to  $\gamma$ -brass-type (721)



The thermal stability of the 60 h milled HEA powder has been investigated using DSC at a heating rate of  $50 \text{ K min}^{-1}$ , and the corresponding DSC thermogram is shown in Fig. 4. It is evident from the DSC thermogram that there are three exothermic events at T1, T2 and T3 and two endothermic events at T4 and T5. The exothermic event at T1 lies over a large range of temperatures, i.e.  $\sim 350 \text{ }^\circ\text{C}$  (623 K) to  $450 \text{ }^\circ\text{C}$  (723 K), which may be attributed to the diffusive transformation of the BCC phase to any complex intermetallic phase. The second exothermic event at T2 occurs at a temperature of  $710 \text{ }^\circ\text{C}$  (983 K), which may be attributed to the diffusive transformation of any complex phase to other intermetallic phases. The nature of this transformation will become clear from the XRD pattern of the heat-treated powdered sample at  $400 \text{ }^\circ\text{C}$ ,  $600 \text{ }^\circ\text{C}$ , along with the SPSed HEA sample, as mentioned below. Both of the thermal events may represent a single transformation which is diffusive in nature and starts at a lower temperature when the atoms have enough kinetic energy of diffusion. However, the kinetics of the transformation becomes fastest at T2. The third exothermic/ endothermic event near T3 is seen at a temperature of  $\sim 960 \text{ }^\circ\text{C}$  (1233 K) and may be attributed to the partial dissolution of  $\text{MgCu}_2$  in  $\gamma$ -brass-type phase. An endothermic event T4, seen at a temperature of  $\sim 960 \text{ }^\circ\text{C}$ , corresponds to the melting of the remaining  $\text{MgCu}_2$  phase. The fifth and the last thermal event at T5 is endothermic and corresponds to the melting of these equiatomic HEA powder at a temperature of  $1170 \text{ }^\circ\text{C}$  (1443 K). Although the thermal events have not been correlated with in situ XRD data, the phase transformation is predicated on the basis of phase evolution of heat-treated ( $400 \text{ }^\circ\text{C}$ ,  $600 \text{ }^\circ\text{C}$ ) and SPSed HEA powder for 15 min at  $900 \text{ }^\circ\text{C}$  (1173 K) as shown in Figs. 6, 7, 8, respectively.

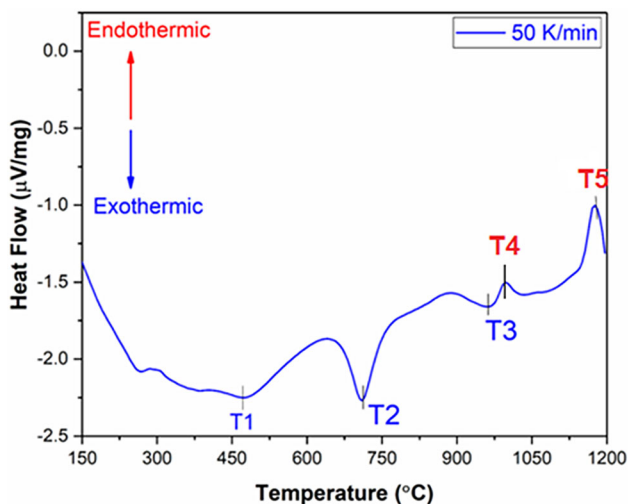


Fig. 4 DSC thermogram of MgAlMnFeCu HEA MA for 60 h

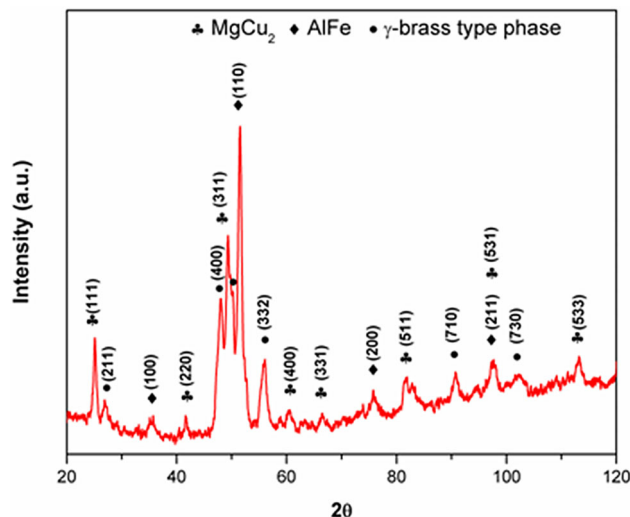


Fig. 5 Phases evolved in MgAlMnFeCu HEA after heat treating the sample at  $400 \text{ }^\circ\text{C}$

Figure 5 shows the evolution of phases after annealing the vacuum-sealed (Quartz tube) as-milled powder at  $400 \text{ }^\circ\text{C}$  (673 K) for 2 h. The XRD pattern of the heat-treated MgAlMnFeCu HEA shows the formation of  $\text{MgCu}_2$  and B2 (AlFe-type) intermetallic phases due to the diffusive transformation of the BCC phase formed in as-milled condition.  $\text{MgCu}_2$  ( $a = 7.02 \pm 0.02 \text{ \AA}$ ) is cubic Laves phase (C15) while B2 is a AlFe-type phase. The  $\gamma$ -brass-type phase present in the as-milled condition is stable up to this temperature.

Figure 6 shows the phases evolved due to the heat treatment of the as-milled HEA powder at  $600 \text{ }^\circ\text{C}$  for 2 h. Indexing the XRD peaks shows that all the phases present at  $400 \text{ }^\circ\text{C}$  are intact except for the change in the amount. The volume fraction of  $\gamma$ -brass-type phase increases

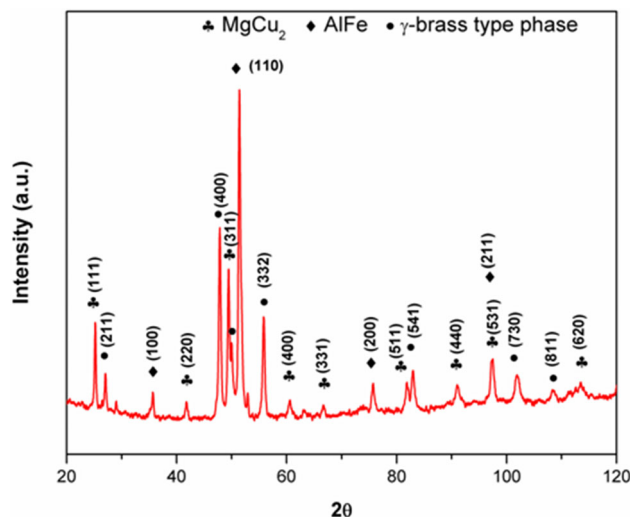


Fig. 6 Phases evolved in MgAlMnFeCu HEA after heat treating the sample at  $600 \text{ }^\circ\text{C}$

slightly compared to the as-milled condition. Comparing both Figs. 5 and 6, we can conclude that the first peak in the DSC thermogram represents a transformation of the BCC phase to MgCu<sub>2</sub>-type and B2 (AlFe-type) intermetallics. At the temperature T1, the diffusive transformation starts. However, the kinetics of the transformation becomes fast at T2. This explains as to why the shape of the heat event at T1 is shallow and that at T2 becomes quite sharp.

Figure 7 shows the evolution of phases after SPS of the 60 h milled MgAlMnFeCu HEA powder at 900 °C (1173 K) for 15 min at 50 MPa pressure. The XRD pattern of SPSed MgAlMnFeCu HEA sample in Fig. 8 shows the significant reduction in the intensity of the MgCu<sub>2</sub> and the increase in the phase fraction of the  $\gamma$ -brass-type phase. The enlarged XRD pattern shown in the inset window indicates the coexistence of B2 (AlFe-type) and MgCu<sub>2</sub>-type intermetallic phases along with a significant volume fraction of the  $\gamma$ -brass-type phase. The reduction in the amount of MgCu<sub>2</sub> in the sample may be due to the melting of the MgCu<sub>2</sub> phase having a melting point of 820 °C [38].

The area selected for the elemental mapping of SPSed HEA is marked in Fig. 8a, while Fig. 8b represents the overall elemental distribution within the selected area of the microstructure. SEM–EDS chemical composition of an individual element within the selected area is shown in Fig. 8c. It is evident from Fig. 8c that the bright region in the SPSed MgAlMnFeCu HEA is rich in Mn and Fe and lean in Al, Mg and Cu.

The bulk density, hardness and compressive strength of the MgAlMnFeCu SPSed HEA are reported in Table 3. It is clear from Table 3 that the relative density of spark plasma sintered HEA is  $\sim 4.94 \text{ g cc}^{-1}$ , which is

comparable to that of conventional alloys prepared using liquid metallurgy route. The density of MgAlMnFeCu HEA with cost-effective alloying elements is better than those of LDHEAs reported in the literature [39]. The bulk hardness and microhardness of these LDHEAs are reported in Table 3. The microhardness of these alloys has been found to be  $\sim 5.06 \text{ GPa}$  with a standard deviation of 0.013 GPa. The hardness of this HEA is even better than that of commercially available alloy systems. The engineering stress vs. engineering strain diagram is shown in Fig. 9, under compressive loading at a strain rate of  $1.8 \times 10^{-3} \text{ s}^{-1}$ . It is clear from Fig. 9 and Table 3 that the compressive yield strength and ultimate tensile strength of these alloys have been evaluated to be, respectively, 1612 MPa and 1792 MPa with very nominal ductility. The failure strain is  $\sim 6.4\%$  and may be attributed to the brittle nature of the fracture occurring as a consequence of ordered B2 (AlFe-type) and MgCu<sub>2</sub>-type phase formation during sintering.

## 4 Discussion

The phase evolution during MA may be explained on the basis of various thermodynamic properties for MgAlMnFeCu HEA. The enthalpy of mixing ( $\Delta H_{\text{mix}}$ ) of binary alloy systems of the constituent elements is presented in Table 4. The enthalpy of mixing for a few binary systems is negative and has a tendency for the formation of intermetallic phases. The highly negative enthalpy of mixing between binary elements such as Al–Fe ( $-11 \text{ kJ mol}^{-1}$ ) and Al–Mn ( $-19 \text{ kJ mol}^{-1}$ ) [40] favours the formation of intermetallic compounds between these elements and is thermodynamically more favourable. Thus, the major fraction of the microstructure consists of B2 (AlFe-type) and  $\gamma$ -brass-type intermetallic phase in SPSed samples, which can be seen in Figs. 5 and 8. Also, Table 5 shows that MgAlMnFeCu HEA does not satisfy the criteria laid down by Zhang et al. [41] for the formation of a single disordered phase solid solution. Zhang et al. [41] have given three necessary criteria for the formation of single-phase solid solution as (i)  $\Delta S_{\text{conf}} \geq 13.38 \text{ J mol}^{-1} \cdot \text{K}^{-1}$ , (ii)  $-10 \text{ kJ mol}^{-1} < \Delta H_{\text{mix}} < 5 \text{ kJ mol}^{-1}$ , (iii)  $\delta < 6.6\%$ . The formation of two phases with different crystal structures despite a comparatively large scatter in the atomic radii of the elements may be due to the presence of high configurational entropy in the HEA. Here, it is important to note that the MgAlMnFeCu HEA system has two elements (Al, Cu) with FCC structure, one (Fe) with BCC structure, one (Mn) with complex cubic structure (close to  $\gamma$ -brass-type) and one (Mg) with HCP structure. It is worth mentioning that  $\alpha$ -Mn has a complex cubic structure, which exhibits various polymorphic transformations as a function of temperature. The initial structure of the phases formed in

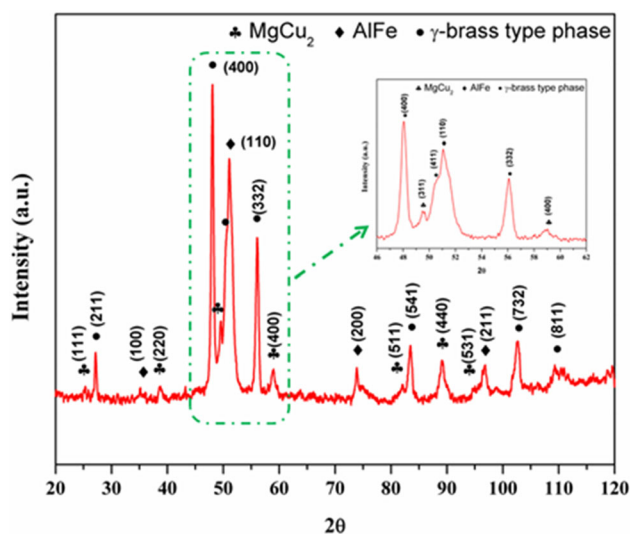


**Fig. 7** Phase evolution of MgAlMnFeCu HEA after SPS; a blown-up image of phase evolved during SPS



**Fig. 8** SEM micrograph of MgAlMnFeCu **a** spark plasma sintered at 900 °C and showing area of elemental mapping; **b** distribution of all the elements within the selected area; **c** SEM–EDS chemical composition of individual elements corresponding to the selected area in **a**; **d–h** individual elemental distribution within the selected window

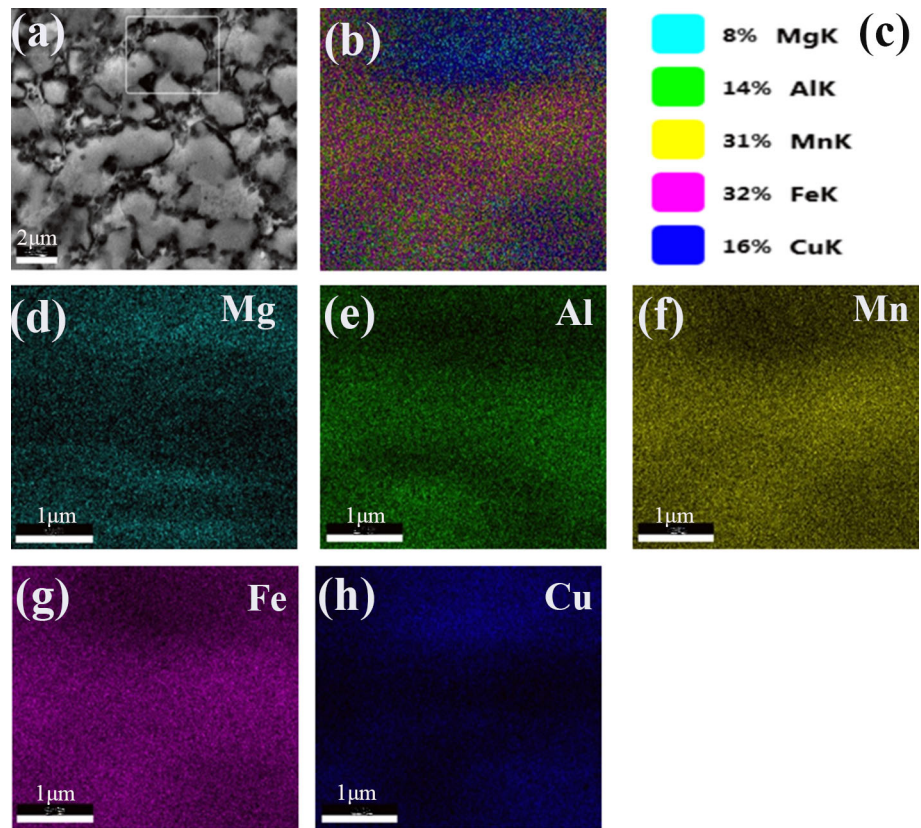


**Table 3** Density, hardness and compressive strength of MgAlMnFeCu HEA

| Bulk density ( $\text{g}\cdot\text{cm}^{-3}$ ) |  |  | Hardness (GPa)   | Compressive strength               |                             |                                 |
|--|--|--|------------------|------------------------------------|-----------------------------|---------------------------------|
| Theoretical density ( $\rho_{\text{the}}$ )    | Experimental density ( $\rho_{\text{exp}}$ ) | Relative density ( $\rho_{\text{exp}}/\rho_{\text{the}}$ ) | Microhardness    | $\sigma_{(0.2) \text{ CYS}}$ (MPa) | $\sigma_{\text{CUS}}$ (MPa) | Failure strain ( $\epsilon_f$ ) |
| 4.960  | $4.946 \pm 0.13$                             | 99.80%   | $5.06 \pm 0.013$ | 1612                               | 1792                        | ~6.4%                           |

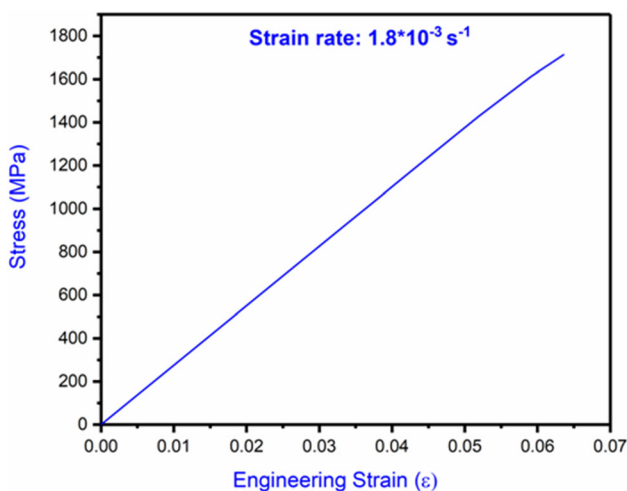


**Fig. 9** Compressive stress–strain plot of MgAlMnFeCu HEA spark plasma sintered at 900 °C for 15 min

HEA seems to correspond to that of the constituent elements having higher melting temperatures, namely Fe and  $\alpha$ -Mn, which serve as host lattices for dissolving the other lower melting elements, as given in Table 1. Thus, positive enthalpy of mixing and the large atomic size difference ( $\delta$ ) leads to the formation of two solid solution phases  $\alpha$ -Fe-type BCC and  $\gamma$ -brass-type phase after MA for 60 h. After doing SPS of prepared HEA, one  $\gamma$ -brass-type structure along with the formation of B2 (AlFe-type) and  $\text{MgCu}_2$ -type intermetallic phases are obtained. In addition to the above-mentioned criteria by Zhang et al. [41], Guo and Liu et al. [42] have suggested an additional criterion based on valence electron concentration (VEC) for the formation of a single-phase solid solution. According to this criterion, for  $\text{VEC} > 8.0$ ,  $6.87 < \text{VEC} < 8.0$  and  $\text{VEC} < 6.87$  lead to the formation FCC structure, mixture of FCC and BCC structures and BCC structure, respectively. Valence

**Table 4** Chemical enthalpy of mixing ( $\Delta H_{ij}^{\text{mix}}$ , kJ/mol) of atomic pairs for MgAlMnFeCu high-entropy alloy, following the Miedema's approach

| Alloys                                  | AlCu | AlFe | AlMn | AlMg | CuFe | CuMn | CuMg | FeMn | FeMg | MnMg |
|---|------|------|------|------|------|------|------|------|------|------|
| $\Delta H_{ij}^{\text{mix}}$ , (kJ/mol) | – 1  | – 11 | – 19 | – 2  | 13   | 4    | – 3  | 0    | 24   | 15   |

**Table 5** Calculated thermodynamic and physical parameter of MgAlMnFeCu HEA

| $\Delta H_{\text{mix}}$ (kJ/mol) | $\Delta S_{\text{conf}}$ (J/mol.K) | Tm (K) | $\Omega$ | $\delta$ (%) | VEC |
|----------------------------------|------------------------------------|--------|----------|--------------|-----|
| 2.82                             | 13.38                              | 1309   | 6.2      | 9.28         | 6.2 |

electron concentration is calculated as weighted average number of total electrons (including d electrons) present in the valence band of the elements in the alloy. The values of VEC are mentioned in Table 5, which suggests the likelihood of the formation of BCC crystal structure and is in line with the criteria suggested by Guo and Liu et al. [42]. Yang and Zhang [43] proposed two criteria for the formation of a single-phase solid solution, namely 'δ' and 'Ω'. For the formation of a single-phase solid solution, the value of δ is less than 6.6% and Ω is greater than 1.1. Although the value of Ω is ~ 6.2, which is well within the above limit, the value of δ is outside the limit, as seen in Table 3. Therefore, the formation of a single solid solution phase is not expected. In the present investigation, two phases (α-Fe-type BCC and γ-brass-type α-Mn) are present in the HEA after 60 h of milling, while two other intermetallics (MgCu<sub>2</sub>-type and B2 (AlFe-type)) and γ-brass-type phases are also observed after SPS.

The sequence of evolution of phases during milling of MgAlMnFeCu HEA can be summarized as follows:

Pre-mixed elemental powders of Al + Cu + Fe + Mn + Mg (0 h)

→ Fe + Mn + Cu + Al

+ Mg (minor peak disappears) (5h milling)

→ Fe + Mn + Cu + Al (significant broadening)

+ Mg (disappear) (10 h milling)

→ Fe + Mn + Cu (significant broadening)

+ Al (disappear) (20 h milling)

→ BCC(Fe) + Complex cubic(Mn)

+ Cu (disappear) (30 h milling)

→ BCC(Fe) (reduction in crystallite size and increase in strain)

+ γ – brass type

(α – Mn) (disappearance of minor peaks) (60 h milling)

It is evident from experimental results that the MgAlMnFeCu HEA milled for 60 h forms two types of

solid solutions as BCC (α-Fe) and γ-brass-type (α-Mn). The sequence of phase evolution is dependent on the physical parameters, as mentioned in Table 1 for the individual elements in the equiatomic composition. The sequence mainly depends upon the melting point, atomic radii and the self-diffusion coefficient. The elements with higher melting points usually act as a host lattice for HEAs as these elements have higher bond strength and stability compared to elements with a low melting point. The self-diffusion coefficient also plays a vital role in dictating the sequence of phase evolution. The sequence of phase evolution during the MA of MgAlMnFeCu HEA is dictated by all the above parameters. The melting point of Fe is highest among all the other elements used. Similarly, the self-diffusion coefficient of Mg is highest, and for Mn, it is lowest. During the systematic investigation of phase evolution during MA of AlCoCrFeMnNi, AlCoCrFeNi and AlCoCrFeNiTi, Shivam et al. [9–11] have reported the role of the melting point of individual elements for preferential affinity to form host lattice. The sequence mainly depends upon the bond strengths of the elements in the HEA. Similarly, they have also reported the minor phases of Mn along with the Fe and Cr host lattice after completion of MA. In line with the present investigation, Maulik et al. [34] have reported the formation of BCC and FCC phases in AlFeCuCrMg<sub>x</sub> (x = 0, 0.5) HEA. They further reported the formation of two BCC phases with an increase in the mole fraction of Mg (x = 1.0, 1.7). Maulik et al. [34] also postulated the sequence of phase evolution based on the bond strength as a function of melting point, atomic radii and self-diffusion coefficient. The self-diffusion coefficient (D) follows the sequence: D(Mn) < D(Fe) < D(Cu) < D(Al) < D(Mg) as mentioned in Table 1. Although the melting point of Mn is less than that of Fe, it can maintain its identity even after 60 h of MA and accommodating other elements.

The LDHEA with bulk density and relative density of  $4.94 \text{ g cc}^{-1}$  and 99.80%, were achieved by the SPS technique. The high hardness and compressive yield strength may be attributed to the solid solution strengthening and precipitation of intermetallics. In the present investigation, it is mainly due to the evolution of AlFe and MgCu<sub>2</sub> intermetallic leading to high hardness and compressive yield strength with a failure strain of  $\sim 6.4\%$ . In the literature, an increase in the mechanical properties is mainly attributed to the formation of various intermetallic particles, such as CuMg<sub>2</sub>, MgCu<sub>2</sub>,  $\sigma$ -phase corresponding to Fe–Cr and ordered AlFe-type phases [34, 35]. The hardness and strength of AlFeCuCrMg<sub>x</sub> ( $x = 0, 0.5, 1.0, 1.7$ ) HEA increases with increasing Mg content, as the phase fraction of ordered AlFe increases. However, further investigation is required to improve the ductility and fracture toughness through suitable processing techniques or further alloy addition.

## 5 Conclusions

The present investigation on MgAlMnFeCu LDHEA leads us to the following conclusions.

- Mechanically alloyed MgAlMnFeCu equiatomic powders after 60 h of milling form a mixture of two solid solution phases, namely BCC phase having lattice parameter close to that of  $\alpha$ -Fe structure ( $a = 2.87 \pm 0.02 \text{ \AA}$ ) and  $\gamma$ -brass-type phase having lattice parameter close to that of  $\alpha$ -Mn ( $a = 8.92 \pm 0.03 \text{ \AA}$ )-type structure which can also be considered as solid solution of  $\alpha$ -Mn.
- The ratio of  $-T\Delta S/\Delta H$  ( $\Omega$ ) is  $\sim 6.2$ , which is in the range of solid solution forming HEAs, as reported in the literature. The VEC value of 6.2 for this alloy indicates the formation of a single BCC phase.  $\delta$  (9.2%) acts as the dominating factor, not forming a single solid solution phase.
- The HEA is stable up to  $\sim 350 \text{ }^\circ\text{C}$  (623 K), which then undergoes a diffusional transformation of the BCC phase resulting in the formation of B2 (AlFe-type) and MgCu<sub>2</sub> Laves phase accompanied by the formation of additional  $\gamma$ -brass-type phase.
- Consolidated and spark plasma sintered pellet of this HEA shows high hardness (5.06 GPa) and high compressive yield strength (1612 MPa) at relatively low density ( $4.94 \text{ g cc}^{-1}$ )

**Acknowledgments** The authors would like to thank Profs. S Lele, R K Mandal, B S Murty and Dr. B Mukherjee for many stimulating discussions. The authors also thank Dr. R Manna for extending the facilities of the Advanced Research Centre for Iron and Steel (ARCIS) as its Coordinator.

## References

1. Cantor B, Chang I T H, Knight P, Vincent A J B, *Mater Sci Eng A* **375–377** (2004) 213 <https://doi.org/10.1016/j.msea.2003.10.257>.
2. Yeh J W, Chen S K, Lin S J, Gan J Y, Chin T S, Shun T T, Tsau C H, Chang S Y, *Adv. Eng. Mater.* **6** (2004) 299 <https://doi.org/10.1002/adem.200300567>.
3. Senkov O N, Miracle D B, Chaput K J, and Cousin J P, *J Mater Res* **33** (2018) 3092 <https://doi.org/10.1557/jmr.2018.153>.
4. Gorsse S, Miracle D B, and Senkov O N, *Acta Mater.* **135** (2017) 177 <https://doi.org/10.1016/j.actamat.2017.06.027>.
5. Miracle D B, and Senkov O N, *Acta Mater.* **122** (2017) 448 <https://doi.org/10.1016/j.actamat.2016.08.081>.
6. Gao M C, *JOM.* **67** (2015) 2251 <https://doi.org/10.1007/s11837-015-1609-z>.
7. Zhang Y, Zuo T T, Tang Z, Gao MC, Dahmen K A, Liaw P K, Lu Z P, *Prog Mater Sci* **61** (2014) 1 <https://doi.org/10.1016/j.pmatsci.2013.10.001>.
8. Yadav T P, Mukhopadhyay S, Mishra S S, Mukhopadhyay N K, Srivastava O N, *Philos Mag Lett* **97** (2017) 494 <https://doi.org/10.1080/09500839.2017.1418539>.
9. Shivam V, Basu J, Shadangi Y, Singh M K, Mukhopadhyay N K, *J Alloys Compd* **757** (2018) 87 <https://doi.org/10.1016/j.jallcom.2018.05.057>.
10. Shivam V, Basu J, Pandey V K, Shadangi Y, and Mukhopadhyay N K, *Adv Powder Technol.* **29** (2018) 2221 <https://doi.org/10.1016/j.apt.2018.06.006>.
11. Shivam V, Shadangi Y, Basu J, and Mukhopadhyay N K, *J. Mater. Res.* **34** (2019) 787 <https://doi.org/10.1557/jmr.2019.5>.
12. Sriharitha R, Murty B S, and Kottada R S, *Intermetallics* **32** (2013) 119 <https://doi.org/10.1016/j.intermet.2012.08.015>.
13. Singh S, Wanderka N, Murty B S, Glatzel U, and Banhart J, *Acta Mater* **59** (2011) 182 <https://doi.org/10.1016/j.actamat.2010.09.023>.
14. Mukhopadhyay N K, *Curr. Sci.* **109** (2015) 665.
15. Pandey V K, Shivam V, Sarma B N, and Mukhopadhyay N K, *Mater. Res. Express.* **6** (2020) 1265b9 <https://doi.org/10.1088/2053-1591/ab618f>.
16. Shivam V, Sanjana V, Mukhopadhyay N K, *Trans. Indian Inst. Met* **73** (2020) 821 <https://doi.org/10.1007/s12666-020-01892-1>.
17. Murty B S, Yeh J W, Ranganathan P P, and Bhattacharjee S., *High-Entropy Alloys*, 2nd Edition, Elsevier, 2019. <https://www.elsevier.com/books/high-entropy-alloys/murty/978-0-12-800251-3>.
18. Steurer W, *Mater. Charact.* **162** (2020) 110179 <https://doi.org/10.1016/j.matchar.2020.110179>.
19. Kokai T, Yachu Y, Chienchang J, Tsungshune C, Chewei T, and Jienwei Y, *Sci China Tech Sci.* **61** (2018) 184 <https://doi.org/10.1007/s11431-017-9073-0>.
20. Yang X, Chen S Y, Cotton J D, and Zhang Y, *JOM.* **66** (2014) 2009. <https://doi.org/10.1007/s11837-014-1059-z>.
21. Youssef K M, Zaddach A J, Niu C, Irving D L, and Koch C C, *Mater Res Lett* **3** (2014) 95 <https://doi.org/10.1080/21663831.2014.985855>.
22. Gao M C, Zhang B, Guo S M, Qiao J W, and Hawk J A, *Metal Mater Trans A* **47** (2016) 3322. <https://doi.org/10.1007/s11661-015-3091-1>.
23. Li H F, Xie X H, Zhao K, Wang Y B, Zheng Y F, Wang W H, and Qin L, *Acta Biomater.* **9** (2013) 8561. <https://doi.org/10.1016/j.actbio.2013.01.029>.
24. Li R, Gao J C, and Fan K, *Mater Sci Forum* **650** (2010) 265. <https://doi.org/10.4028/www.scientific.net/msf.650.265>.
25. Li R, Gao J C, and Fan K, *Mater Sci Forum* **686** (2011) 235. <https://doi.org/10.4028/www.scientific.net/msf.686.235>.

26. Feng R, Gao M C, Zhang C, Guo W, Poplawsky J D, Zhang F, Hawk J A, Neuefeind J C, Ren Y, and Liaw P K, *Acta Mater* **146** (2018) 280 <https://doi.org/10.1016/j.actamat.2017.12.061>.
27. Chen Y L, Tsai C W, Juan C C, Chuang M H, Yeh J W, Chin T S, and Chen S K, *J. Alloys Compd* **506** (2010) 210 <https://doi.org/10.1016/j.jallcom.2010.06.179>.
28. Sanchez J M, Vicario I, Albizuri J, Guraya T, and Garcia J C, *J Mater Res Technol* **8** (2019) 795. <https://doi.org/10.1016/j.jmrt.2018.06.010>.
29. Senkov O N, Senkova S V, Woodward C, Miracle D B, *Acta Mater.* **61** (2013) 1545. <https://doi.org/10.1016/j.actamat.2012.11.032>.
30. Senkov O N, Senkova S V, Miracle D B, and Woodward C, *Mater Sci Eng A* **565** (2013) 51. <https://doi.org/10.1016/j.msea.2012.12.018>.
31. Stepanov N D, Shaysultanov D G, Salishchev G A, and Tikhonovsky M A, *Mater Lett* **142** (2015) 153. <https://doi.org/10.1016/j.matlet.2014.11.162>.
32. Stepanov N D, Yurchenko N Y, Sokolovsky V S, Tikhonovsky M A, and Salishchev G A, *Mater. Lett.* **161** (2015) 136. <https://doi.org/10.1016/j.matlet.2015.08.099>.
33. Khanchandani H, Sharma P, Kumar R, Maulik O, and Kumar V, *Adv Powder Technol.* **27** (2016) 289. <https://doi.org/10.1016/j.apt.2016.01.001>.
34. Maulik O, and Kumar V, *Mater Charact* **110** (2015) 116. <https://doi.org/10.1016/j.matchar.2015.10.025>.
35. Maulik O, Kumar D, Kumar S, Fabijanic D M, and Kumar V, *Intermetallics* **77** (2016) 46. <https://doi.org/10.1016/j.intermet.2016.07.001>.
36. Miedema A R, de Châtel P F, de Boer F R, *Phys. B + C* **100** (1980) 1. [https://doi.org/10.1016/0378-4363\(80\)90054-6](https://doi.org/10.1016/0378-4363(80)90054-6)
37. Williamson G, and Hall W, *Acta Metall* **1** (1953) 22 [https://doi.org/10.1016/0001-6160\(53\)90006-6](https://doi.org/10.1016/0001-6160(53)90006-6).
38. Mao P, Yu B, Liu Z, Wang F, and Ju Y, *Trans Nonferrous Met Soc China* **24** (2014) 2920. [https://doi.org/10.1016/s1003-6326\(14\)63427-0](https://doi.org/10.1016/s1003-6326(14)63427-0).
39. Maulik O, Kumar D, Kumar S, Dewangan S K, and Kumar V, *Mater. Res. Express.* **5** (2018) 052001. [10.1088/2053-1591/aabbca](https://doi.org/10.1088/2053-1591/aabbca).
40. Chen Y L, Hu Y H, Hsieh C A, Yeh J W, and Chen S K, *J Alloys Compd* **481** (2009) 768. <https://doi.org/10.1016/j.jallcom.2009.03.087>.
41. Zhang Y, Zhou Y J, Lin J P, Chen G L, and Liaw P K, *Adv Eng Mater* **10** (2008) 534. <https://doi.org/10.1002/adem.200700240>.
42. Guo S, and Liu C T, *Prog Nat Sci Mater Int* **21** (2011) 433 [https://doi.org/10.1016/s1002-0071\(12\)60080-x](https://doi.org/10.1016/s1002-0071(12)60080-x).
43. Yang X, and Zhang Y, *Mater Chem Phys* **132** (2012) 233 <https://doi.org/10.1016/j.matchemphys.2011.11.021>.

**Publisher's Note** Springer Nature remains neutral with regard to jurisdictional claims in published maps and institutional affiliations.